AIAA JOURNAL
Vol. 47, No. 1, January 2009

High-Resolution Reynolds-Averaged Navier–Stokes Flow Predictions over Axisymmetric Bodies with Tapered Tails

T. L. Jeans*
U.S. Air Force Academy, Colorado Springs, Colorado 80840
G. D. Watt†
Defence Research and Development Canada—Atlantic, Dartmouth, Nova Scotia B2Y 3Z7, Canada
and
A. G. Gerber,‡ A. G. L. Holloway,§ and C. R. Baker¶
University of New Brunswick, Fredericton, New Brunswick E3A 6S3, Canada

DOI: 10.2514/1.30911

A comprehensive computational study is performed on two slender axisymmetric streamlined bodies with tapered tails in translation at incidence up to 30 degrees at Reynolds numbers up to 23×10^6. The computations are verified with the aid of a parameterized scripted hybrid mesh adapted to the separated wake. They are validated using experimental overall force and longitudinal force distribution measurements from a wind tunnel and towing tank. Overall force predictions using the Reynolds stress and shear stress transport turbulence models are within experimental uncertainty up to 25- and 15-degree incidences, respectively. A comprehensive study is made of the skin friction, surface pressure, and separation lines based on the computational results. Flowfield vorticity from the computations is used to evaluate slender-body assumptions applied to hydrodynamic impulse theory. Force distribution predictions from this theory agree well with direct integration of pressure and wall shear stress for these viscous separated flows.

Nomenclature

a	=	local body radius
C_{Fy}	=	normal force coefficient, $F_y/(q_\infty l^2)$
$\lvert C_f \rvert$	=	skin-friction magnitude, $\lvert\tau_w\rvert/q_\infty$
C_{Mz}	=	pitching-moment coefficient about the center of buoyancy, $M_z/(q_\infty l^3)$
C_n	=	normal force per unit length coefficient, $(dF_y/dx)/(q_\infty l)$
C_{pc}	=	crossflow pressure coefficient, $(p - p_\infty)/q_\infty \sin^2\alpha$
F_x, F_y, F_z	=	axial, normal, and lateral forces in body-fixed coordinates
F_1, F_2	=	turbulence-model blending factors
M_x, M_y, M_z	=	rolling, yawing, and pitching moment in body-fixed coordinates
$i_Y(x)$	=	axial distribution of hydrodynamic impulse per unit length in the y-axis direction
k	=	turbulence kinetic energy
l	=	body length
P	=	shear production of turbulence
p	=	pressure
q_∞	=	freestream dynamic pressure, $1/2\rho\lvert U_\infty^2\rvert$
Re	=	Reynolds number based on body length, $\lvert U_\infty\rvert l/\upsilon$
t	=	time
$\boldsymbol{U}$	=	velocity vector
$\boldsymbol{U}o$	=	body velocity vector
$\boldsymbol{U}_\infty$	=	freestream velocity vector
u, v, w	=	velocity components in the x, y, and z directions
v_t	=	shear stress eddy viscosity
X, Y, Z	=	inertial axes coordinates
x, y, z	=	body-fixed axes coordinates
α	=	angle of incidence
α, β, σ	=	turbulence-model constants
Γ	=	circulation
δ	=	identity matrix
ε	=	turbulent eddy dissipation
θ	=	circumferential angle measured from the windward side to the leeward side
λ	=	longitudinal distance aft from the nose
μ	=	dynamic viscosity
μ_T	=	turbulent viscosity
ρ	=	fluid density
υ	=	kinematic viscosity
σ, σ^*	=	turbulent Prandtl numbers
$\boldsymbol{\tau}_w$	=	wall shear stress
ω	=	turbulence frequency
$\boldsymbol{\omega}$	=	vorticity

Subscript

i	=	inertial coordinate frame

Received 9 March 2007; revision received 25 August 2008; accepted for publication 12 September 2008.

*Visiting Researcher, Department of Aeronautics; tiger.jeans.ctr@usafa.edu. Member AIAA.
†Defense Scientist, P.O. Box 1012; george.watt@drdc-rddc.gc.ca.
‡Associate Professor, Department of Mechanical Engineering; agerber@unb.ca.
§Professor, Department of Mechanical Engineering; holloway@unb.ca.
¶Graduate Student, Department of Mechanical Engineering; w2jc1@unb.ca.

I. Introduction

HYDRODYNAMICISTS are concerned with predicting the performance, stability, and safe operating limits of the vehicles they analyze. This requires the ability to predict the hydrodynamic forces experienced by the vehicle. Three distinct approaches currently exist for determining these forces: captive-model experiments, computational fluid dynamics (CFD), and

semitheoretical force-estimation methods. Captive-model experiments provide the most comprehensive representation of the flow physics, but they are time-consuming and expensive, making them impractical for most applications. Furthermore, experimental methods are limited in the amount of flow detail that can be extracted. Computational studies generally contain serious limitations in their representation of the flow physics, but they are relatively inexpensive and provide practically unlimited flow detail. This paper presents high-resolution benchmark computational studies of two unappended submarine model shapes that have been studied experimentally at high Reynolds numbers. This provides the unique opportunity for experimental validation of the Reynolds-averaged Navier–Stokes (RANS) method and its inherent turbulence models for this class of body shape. No comparable study in conjunction with verification and validation currently exists in the literature for axisymmetric bodies with tapered tails at these Reynolds numbers. These relatively simple geometries are challenging for CFD because they lack edges that fix separation, and the overall hydrodynamic force on them, even at incidence, results purely from viscous effects (it is zero in a potential flow [1]). The CFD-predicted flowfields about these bodies are used to assess slender-body theory assumptions applied to viscous flows. This provides the theoretical basis for developing computationally efficient semitheoretical force-estimation methods that are required for faster-than-real-time maneuvering simulations.

Underwater-vehicle forces are typically estimated by building them up on a component-by component basis by starting with the streamlined hull, superimposing appendage forces and their interference effects, and adding propulsion. Historically, the hull forces have been the most difficult to model and, unlike airplanes, are among the largest contributor to the total hydrodynamic force. This is especially true when the hull experiences moderate-to-large incidence angles of 15 to 30 deg, which can occur uniformly when blowing ballast or locally along the tail in a tight turn.

A primary result of this paper is the creation of a validated enhanced database consisting of both experimental and CFD data for these axisymmetric streamlined bodies with tapered tails at high incidence and Reynolds numbers. The experimental database consists of previous captive wind-tunnel [2–4] and tow-tank [5] experiments on two unappended submarine hull profiles and is used for validation of the CFD database up to $Re = 23 \times 10^6$. The detail available from the CFD simulations is necessary to our investigation of the hydrodynamic phenomena dominating the flowfield.

Previous CFD studies based on the RANS equations provided good predictions for the steady-state forces on axisymmetric bodies at incidence angles up to 20 deg [6–8] but were unreliable at higher incidence [7]. Therefore, improvements are necessary before CFD results can be confidently used for model development at incidence greater than 20 deg. The current study improves this reliability by developing a specialized mesh adapted to axisymmetric shapes and their wakes. Numerical and turbulence-modeling errors are properly quantified and separated, allowing for proper turbulence-model evaluation and comparison, an additional improvement over previous studies.

The flow topology of a standard axisymmetric body in translation at moderate incidence is shown in Fig. 1. Plotted are surface skin-friction lines and streamlines around the body, colored by total pressure. A key feature of the flow is the separation that forms on the tail at low incidence and migrates noseward as incidence is increased. Even at moderate incidence, the separation is strong and separation sheets roll up into concentrated vortices. Shear layers continually feed these vortices, causing them to grow in both size and strength. The end result is a three-dimensional wake on the body's leeside that consists of two symmetric vortices of opposite sense. An accurate computational model must properly account for these important flow features. Modeling the flow over the tapered tail is critical to determining normal force and pitching moment on these bodies. Such flow features are absent in missile-shaped bodies with truncated bases. The present study contributes to the literature by providing a detailed description of the flow behavior in the tail region.

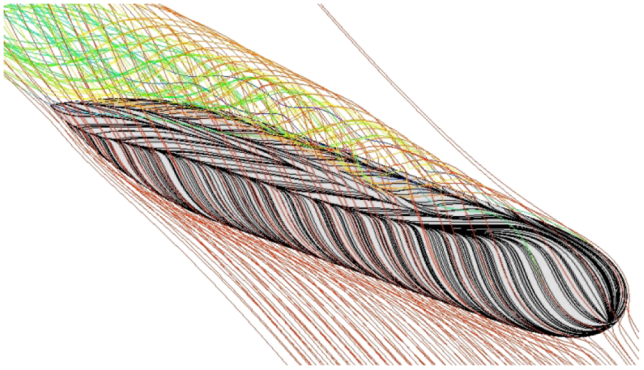

Fig. 1 Flow streamlines for the DRDC-STR hull in translation at 30 deg incidence.

II. Model Geometry Description

The two standard axisymmetric hull shapes studied were the unappended Defence Research and Development Canada (DRDC) static-test-rig (STR) [3] hull and the U.S. Naval Surface Warfare Center Carderock Division Series-58 model 4621 [5] submarine hull. Profiles of both bodies are shown in Fig. 2. The DRDC-STR profile has three distinct regions: the first 20% of the hull is the nose with a Riegels-type D_2 profile, the next 45% is the cylindrical midbody, and the final 36% is the tail section, which has a parabolic profile. The Series-58 model 4621 profile is described by a continuous sixth-order polynomial [5] and differs significantly from the DRDC profile, largely due to its spheroid nose and absence of a constant-radius midbody region. The DRDC-STR and Series-58 model 4621 profiles have length-to-maximum-diameter ratios of 8.75 and 7.34, respectively.

The body forces and moments are calculated relative to the body-fixed coordinate system shown in Fig. 3. The origin is located at the center of buoyancy. The axial, normal, and lateral force components are calculated in the x, y, and z directions, respectively, and the pitching moment is calculated about the z axis. The freestream velocity approaches with an angle of incidence measured in the x–y plane.

III. Related Experimental and Computational Studies

Both the DRDC-STR and Series-58 model 4621 profiles have been previously studied experimentally and computationally. In 1988, experiments were performed on the DRDC-STR hull in the 9 m wind tunnel at the National Research Council of Canada, Institute for Aerospace Research [2,3]. Tests were completed for Reynolds numbers up to 23×10^6 and incidence angles up to 30 deg, and data were corrected for support strut tare and interference [4]. In

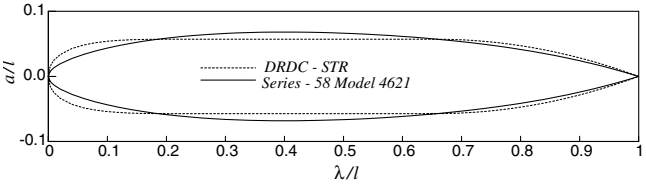

Fig. 2 DRDC-STR and Series-58 model 4621 hull profiles.

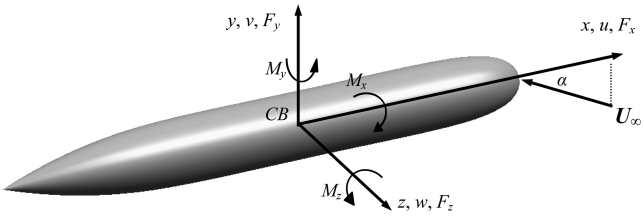

Fig. 3 DRDC-STR hull with body-fixed coordinate axes.

2000, captive-model towing-tank experiments were performed on the Series-58 model 4621 hull in the David Taylor Model Basin at the U.S. Naval Surface Warfare Center [5]. Tests were completed at Reynolds numbers of 4.7×10^6,9.4×10^6, and 11.7×10^6 and incidence angles up to 18 deg. The model was built in segments connected with load-measuring devices so that axial distributions of normal force were measured in addition to overall force. Data from these experiments consist of overall force and moment coefficients, total pressure distributions through the wake region, surface streamlines, and localized segmented force data, all of which are used to validate the current predictions.

Because of the large Reynolds numbers associated with these flows, the only feasible computational methods currently available are RANS or detached eddy simulation (DES). DES differs from RANS in that it implements RANS in the attached boundary layer and large eddy simulation in the separated-flow regions. It has been very successful at modeling extremely unsteady flows at high angles of attack [9–11]. However, for the current study, the flow is relatively steady in that the leeside vortices are stable and vortex bursting or shedding does not occur. Nichols [12] studied the flow over an ogive cylinder at 20 deg incidence and showed very little difference in the development in the leeside vortex using either RANS or DES. In fact, DES has been known to give unreliable predictions for flows with relatively shallow steady separation, due to an ambiguous-grid issue emphasized by Menter and Kuntz [13].

Previous RANS simulations have been completed on the DRDC-STR hull at Reynolds numbers up to 230×10^6 and incidence angles up to 30 deg [8] and on the Series-58 model 4621 hull at a Reynolds number up to 11.7×10^6 and incidence angle up to 18 deg [7]. Baker et al. [8] used a nonaxisymmetric 2.7-million-node mesh, the SST turbulence model, and viscous sublayer meshing, yielding y^+ values less than or equal to 1. This dramatically improved both the discretization and physical modeling used in the RANS predictions over a previous proprietary DRDC study using only 400,000 nodes and wall functions. The high-incidence predictions substantially improved, but surprisingly, the low-incidence predictions also changed substantially. The present study adapts the mesh to the shear layer and leeside vortices to further improve the discretization of the flowfield.

Other computational efforts for axisymmetric bodies at incidence include those by Degani [14], Schiff et al. [15], and Degani and Levy [16]. However, all of these simulations are for missile-shaped bodies that lack the tapered tail section, a significant difference from the bodies in the current study. In addition, these missile studies are concerned with higher angles of incidence for which the vortices are asymmetric and are shed in a periodic fashion.

Allen and Perkins [17] first discovered that when a slender axisymmetric body is pitched through angles of incidence ranging from 0 to 90 deg it experiences four distinct flow patterns. At low angles, the axial flow dominates and the flow remains attached. At intermediate angles, the crossflow causes the boundary layer to separate on the leeside, forming two separation sheets that roll up into two symmetric vortices of opposite rotation. At high angles, these vortices become asymmetric, generating a side force in the z-axis direction. At very high angles of incidence, the crossflow completely dominates and the vortices become unstable and are shed in an unsteady manner.

Lamont [18] performed high Reynolds number experiments on an ogive cylinder at incidence and measured small out-of-plane forces for 20 deg $< \alpha <$ 30 deg, indicating only a small asymmetry over this incidence range. Ericsson and Reding [19] surveyed the literature on high-incidence missile aerodynamics and concluded that the flow characteristics are a function of incidence and slenderness. Based on previous experiments for missile-shaped bodies in the Reynolds number range applicable to underwater vehicles, Ericsson and Reding concluded that for a length-to-diameter ratio of 9, the vortices become asymmetric at incidence angles between 25 and 35 deg and unsteady at incidence angles between 60 and 70 deg. They present the following empirical formula for determining the axial location at which asymmetry first begins: $\lambda = 8.4 a_{\max}/\alpha$. For the DRDC-STR hull at $\alpha = 30$ deg, this formula predicts that the vortices become asymmetric at $\lambda/l = 0.92$; however, for the Series-58 model 4621 body, it predicts that the vortices remain symmetric over the entire body length for the full range of incidence considered. Full field computations were performed for the DRDC-STR hull at $\alpha = 30$ deg and, although a very small asymmetry of the vortices near the tail region was found, the resulting side forces were insignificant. As a consequence, all results presented in this paper are derived from half-body simulations under the assumption of flow symmetry.

IV. Computational Model

The CFD simulations are based on the unsteady RANS equations in their conservative form [20]. Turbulence models are required to close the system of RANS mean flow equations by providing estimates of the Reynolds stresses. The two turbulence models that were used for these simulations were the shear stress transport (SST) model [21] and the baseline Reynolds stress model (BSL-RSM) [22].

The SST model is known to give reliable predictions of two-dimensional flow separation due to adverse pressure gradients [21]. It is a two-equation model that uses an extended Boussinesq relationship to relate the Reynolds stress terms in the RANS equations to the velocity gradients in the flow as follows:

$$-\rho\overline{u_i u_j} = \mu_t\left(\frac{\partial \bar{U}_i}{\partial x_j} + \frac{\partial \bar{U}_j}{\partial x_i}\right) - \frac{2}{3}\rho\delta_{ij} \tag{1}$$

The SST model used is based on the baseline k-ω model developed by Menter [21], which is a blend between the standard k-ε and k-ω models, for which the former is implemented in the outer region and the latter is implemented in the near-wall region. For each region, standard transport equations are solved for either k and ε or k and ω. The eddy viscosity is obtained from

$$v_t = \frac{\mu_t}{\rho} = \frac{a_1 k}{\max(a_1\omega, SF_2)} \tag{2}$$

where S is an invariant measure of the strain rate and F_2 is a blending function. Blending functions are critical to the success of the SST model because they are responsible for the turbulence-model transition between k-ω and the transformed k-ε formulation [21].

The BSL-RSM model is based on solving full transport equations for all six Reynolds stresses and the dissipation rate [22]. This model inherently models the anisotropies in the Reynolds stresses, unlike the two-equation formulations based on Eq. (1). The modeled equations for Reynolds stress transport written in index notation are as follows:

$$\frac{\partial(\rho\overline{u_i u_j})}{\partial t} + \frac{\partial(\rho\bar{U}_k\overline{u_i u_j})}{\partial x_k} = \frac{\partial}{\partial x_k}\left(\left(\mu + \frac{\mu_t}{\sigma^*}\right)\frac{\partial\overline{u_i u_j}}{\partial x_k}\right) - \rho P_{ij} + \frac{2}{3}\beta'\rho\omega k\delta_{ij} - \rho\Pi_{ij} \tag{3}$$

where P_{ij} is the production tensor of Reynolds stress, Π_{ij} is the constitutive relation for the pressure-strain correlation, and σ^* is the turbulent Prandtl number. The BSL-RSM model implements near-wall boundary-layer modeling in the same manner as the SST model.

The CFD simulations were completed using a commercially available program (ANSYS-CFX) based on the RANS equations discretized using a finite-volume/finite-element method [23]. Using collocated control volumes for velocity and scalar equations, full second-order spatial discretization was employed to minimize numerical diffusion. An implicit coupled solver is employed to solve the hydrodynamic (u, v, w, p) equations as a single system [24,25]. Double precision was used throughout to minimize round-off error, an important consideration in the near-wall region, which contains hexahedra elements with aspect ratios as large as 1.9 million because of the high Reynolds number. The additive correction [26] algebraic multigrid [27] procedure was used to accelerate the solution. The governing equations were converged in all simulations until the rms residuals for mass and momentum within the domain were below 1.0×10^{-5}.

To take advantage of the symmetry, only half the streamline body was modeled in the final simulations. The streamlined axisymmetric body is approximately centered in the domain and orientated at the desired incidence relative to the outer boundaries. The advantage of this approach is that the inlet and outlet are normal to the freestream and the opening boundaries are parallel to the freestream. The nominal distance from the body to the outer boundaries is $2l$, which was verified to be sufficient by Baker [28]. The turbulence intensity at the inlet was set to 1% to match experimental conditions. At the outlet, the average static pressure was set to zero. The no-slip wall condition was employed on the hull surface, and the free-slip wall condition was used along the symmetry plane. On the final three outer boundaries, fluid was permitted to enter and leave the domain as required to match the freestream pressure condition.

The current study uses a scripted hybrid mesh consisting of both structured and unstructured mesh cells [29]. Scripting automates and parameterizes the mesh-building process, giving good control and reproducibility for a variety of hull shapes. Hexahedra are used in the dense inner and less dense outer structured grids, and pyramids and tetrahedral are used to transition between them. The dense inner mesh resolves small scales in the boundary-layer and trailing wake regions, whereas larger cells are adequate in the outer flowfield, as shown in Fig. 4. This overall approach provides a low overhead mesh in terms of storage requirements (the element to node ratio is kept reasonably close to 1) and efficient boundary-layer modeling and allows mesh refinement to be localized to key areas without affecting the far field, where less mesh is required.

A substantial effort was made to accurately discretize the leeside vortex and shear layers. The near-body mesh is built from transverse planes constructed at several user-determined axial stations, as shown in Fig. 5 (which is shown much coarser than the actual mesh employed). For the given study, these planes were constructed at $\lambda/l = 0.3$, 0.488, 0.722, 0.85, and 1.0. Parameters are specified at each plane that determines the radial, circumferential, and axial mesh spacing and expansion rates. Mesh characteristics are typically specified at the stern and leeward symmetry planes and then funneled axially into the vortex inception region and compressed circumferentially into the windward region, as shown in Fig. 5.

An illustration of the radial and circumferential node distribution at a given transverse plane along with the critical parameters that determine this distribution is shown in Fig. 6. The radial distribution is built in three stages: stages 1 and 3 are regions of geometric expansion and stage 2 is constant spacing. Three additional parameters (Φ, R_{lee}, and Y_{lee}) are required at each transverse station to ensure proper nodal spacing through the leeside vortex. These parameters are based on the size of the leeside vortex and the separation location, as defined in Fig. 6a.

To ensure that the volume mesh adequately discretized the boundary layer, the first node height was chosen to keep the maximum y^+ value below 0.3. The mesh parameters chosen for the current study resulted in grids ranging from 3 to 8 million nodes, depending on incidence and Reynolds number. In general, the number of nodes increased as incidence or Reynolds number increased.

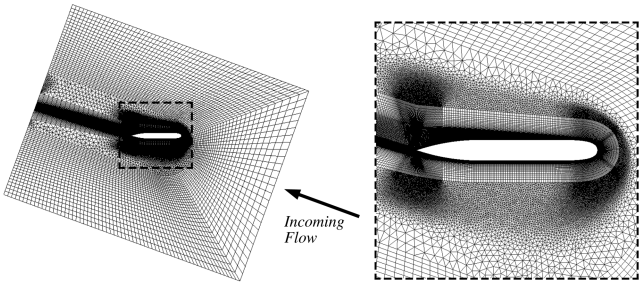

Fig. 4 Symmetry-plane surface mesh highlighting the topology of the hybrid grid.

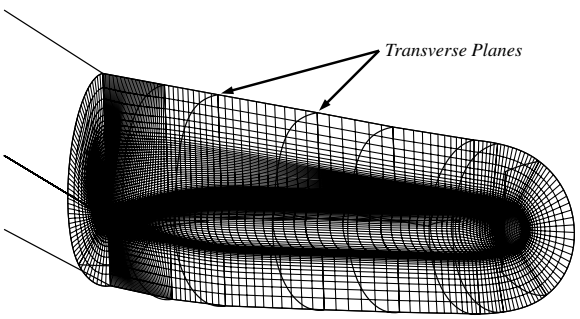

Fig. 5 A coarsened-mesh illustration showing different axial stations with different windward, separation, and leeward circumferential spacing and angular point of separation.

V. Verification and Validation of RANS Predictions

A key advantage of the scripting algorithm is that the mesh can be uniformly scaled using one parameter (mesh density factor), which is desirable for verification [30]. To ensure that mesh-independent solutions were obtained or that discretization error was minimal, RANS simulations were completed for the Series-58 model 4621 hull at $Re = 11.7 \times 10^6$ and $\alpha = 18$ deg for mesh density factors of 0.5, 1.0, and 2.0. This uniformly doubled and halved the number of nodes throughout the domain to within 1% error [30]. A comparison of total normal force and pitching-moment coefficients is shown in Table 1 for both the SST and BSL-RSM turbulence models. This suggests that a mesh-independent solution was obtained using a default mesh density factor of 1.0. This approach uses a constant mesh topology; for example, the ratio of axial to circumferential spacing remains the same throughout the mesh. Using this meshing script, Baker [28] varied the topology by varying local mesh parameters, creating meshes as large as 16 million nodes. He found that the normal force predictions at 30 deg incidence would vary by less than 5%, regardless of where in the flow he chose to increase mesh density. Therefore, we conclude that discretization error for the total integrated normal force and pitching moment is less than 5% for the current simulations.

A list of the RANS simulations completed for the current study is shown in Table 2. Simulations were carried out on the DRDC-STR hull at Reynolds numbers up to 230×10^6 and incidence angles up to 30 deg and on the Series-58 model 4621 hull at Reynolds numbers up to 23×10^6 and incidence angles up to 25 deg. Both the SST and BSL-RSM turbulence models were tested for each shape.

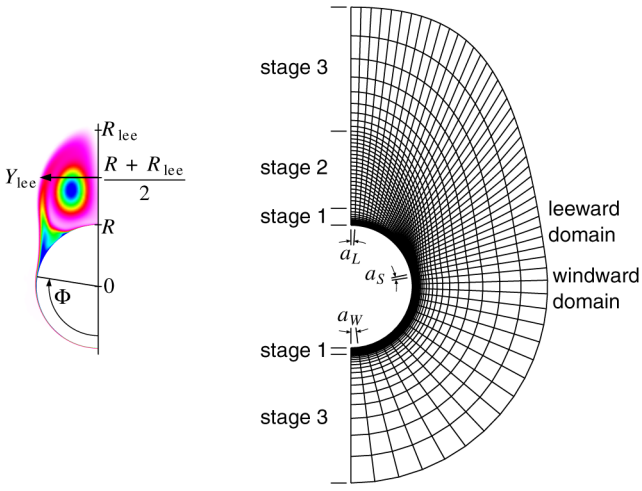

a) Required empirical parameters Φ, R_{lee}, Y_{lee} **b) Station nodal spacing**

Fig. 6 A coarsened-mesh illustration of the radial and circumferential nodal distribution near the body, highlighting the mesh adaption parameters.

Table 1 Comparison of RANS normal force predictions with varying mesh density for the Series-58 model 4621 hull at $Re = 11.7 \times 10^6$ and $\alpha = 18$ deg; all computations were performed on a half-body geometry assuming longitudinal symmetry

Turbulence model	Mesh density	Node count $\times 10^6$	$C_{Fy} \times 10^2$	% diff	$C_{Mz} \times 10^2$	% diff
SST	1.0	4.7	0.5629	N/A	0.3155	N/A
SST	0.5	2.4	0.5621	0.14	0.3153	0.06
SST	2.0	9.3	0.5631	0.02	0.3157	0.07
RSM-BSL	1.0	4.7	0.6454	N/A	0.3018	N/A
RSM-BSL	0.5	2.4	0.6463	0.15	0.3011	0.23
RSM-BSL	2.0	9.3	0.6451	0.04	0.3022	0.12

Table 2 RANS simulations completed for the current study

Profile	$Re \times 10^6$	α, deg	Turbulence model
DRDC-STR	23	5, 10, 15, 20, 25, 30	SST
DRDC-STR	23	10, 15, 20, 30	BSL-RSM
DRDC-STR	230	20	SST
DRDC-STR	11.7	25	SST
Series-58 M4621	11.7	5, 6, 12, 18, 20, 25	SST
Series-58 M4621	11.7	6, 12, 18	BSL-RSM
Series-58 M4621	23, 4.2	20	SST

The primary means of validation for the RANS predictions are comparisons of overall force and moment coefficients with experimental data. Normal force coefficients as a function of incidence are shown in Figs. 7a and 7b for the DRDC-STR and Series-58 model 4621 hulls, respectively. Experimental data are shown for both positive and negative incidence angles and are least-squares-fitted with a seventh-order polynomial in odd powers of α. For the DRDC-STR data, the experimental uncertainty is the band centered on this fit and delimited by the dashed lines. The uncertainty is the result of a conservative analysis in which the magnitudes of all identified uncertainties are summed. Notice that the data were acquired in a high-incidence experiment that did not provide good resolution at low incidence. No uncertainty estimates are available for the Series-58 model 4621 data, but the uncertainty should be less than for the DRDC-STR data, given the smaller incidence range.

At moderate-to-large incidence, both the SST and BSL-RSM models underpredict the normal force. BSL-RSM RANS predictions for the DRDC-STR hull are within experimental uncertainty for $\alpha < 25$ deg, and SST RANS predictions are within experimental uncertainty for $\alpha < 15$ deg. It is more difficult to properly quantify the normal force predictions for the Series-58 model 4621 results, due to the lack of error bars for the experimental data; however, the same trends are clearly present.

Hydrodynamicists are concerned with both the ability to predict the normal force and, for stability analyses, with the slope of this curve through the origin. Thus, we are concerned with the relative difference between predictions and data at each incidence angle. This is best seen by normalizing the RANS data in Figs. 7a and 7b by the least-squares fit to the experimental data, as shown in Figs. 7c and 7d. With discretization error in the current results capped at 5%, Fig. 7c shows that modeling error in the current SST RANS predictions is responsible for an underprediction of experiment in the 20 to 30 deg incidence range. Interestingly, the relative error here does not change much with incidence. The BSL-RSM RANS predictions, which use an anisotropic turbulence model, approximately halve the modeling error at moderate incidence angles and substantially alter the stability derivative at low incidence. Figure 7d shows roughly the same modeling error as in Fig. 7c in the SST and BSL-RSM RANS predictions at moderate incidence. The BSL-RSM model probably improves the stability derivative prediction, but low incidence accuracy in the DRDC-STR and Series-58 model 4621 data, respectively, prevent a definitive assessment.

Figures 8a and 8b compare RANS predictions of pitching-moment coefficients about the center of buoyancy, using the SST and BSL-RSM turbulence models, with experimental data for the DRDC-STR and Series-58 model 4621 hulls, respectively. The differences in the DRDC-STR RANS predictions are not nearly as large as for normal force and, except for the 30 deg BSL-RSM comparison with experiment, all RANS predictions fall within experimental uncertainty. There is a 5 to 10% modeling difference between the SST and BSL-RSM turbulence-model predictions. The Series-58 model 4621 data shows the same level of error in the RANS predictions as the DRDC-STR data. Indeed, the pitching-moment comparisons in Fig. 8b are remarkably similar to the Fig. 7b normal force comparisons. In each, the RANS predictions err toward the inviscid solution (zero normal force and a larger pitching moment), with the BSL-RSM prediction halving the error.

Validation of the Series-58 model 4621 RANS predictions is enhanced by comparison of normal force distributions, as shown in Figs. 9a–9c for $\alpha = 6$, 12, and 18 deg at $Re = 11.7 \times 10^6$. Experimental normal force distributions were determined by cutting the hull into ten sections and reassembling the sections with load cells between them [5]. The general topology of all the normal force distributions is an upward force over the forebody and downward force over the afterbody. Both the SST and BSL-RSM RANS predictions compare favorably with the experiment over the forebody, with the possible exception of the nose itself. However, the RANS simulations overpredict the downward force on the tail, at least at moderate incidence angles. This suggests that the RANS simulations overpredict the pressure recovery on the leeside and the energy loss in the wake is underpredicted. This error is consistently reduced using the improved BSL-RSM turbulence model.

VI. Surface Pressure and Skin-Friction Distributions of CFD Solutions

The skin-friction lines and pressure contours on the axisymmetric body surface derived from the CFD solution of the DRDC Hull at 30 deg incidence are shown in Fig. 10. Longitudinal leeside vorticity at select cross sections is also shown. The skin-friction pattern is steady but complicated by flow separation and the close proximity of the leeside vortices to the body. Separation lines are indicated by the confluence of skin-friction lines, and reattachment lines are indicated by the divergence of skin-friction lines. Typically, one separates the surface into the region upstream and windward of the primary separation line and the region downstream and leeward, which underlies the rotational body wake. The latter region is marked by a complex pattern of reattachment and separation lines but exhibits nearly constant surface pressure. Energy loss lowers the pressure in this wake region and is responsible for the normal force on the body.

Several researchers have previously discussed the qualitative and quantitative nature of the flowfield around slender bodies of revolution at incidence, in particular, the nature of separation. Simpson [31] discussed qualitative traits of three-dimensional separation, Yates and Chapman [32] discussed the related separation kinematics, and Wetzel and Simpson [33] discussed quantitative methods for determining the point of separation on a prolate spheroid. Separation occurs as a result of adverse pressure gradients due largely to the crossflow, and so it is typically referred to as crossflow separation.

BSL-RSM RANS predictions of circumferential surface-pressure distributions are plotted in Fig. 11 for the DRDC hull at $Re = 23 \times 10^6$ and $\alpha = 30$ deg. The windward and leeward sides of the body

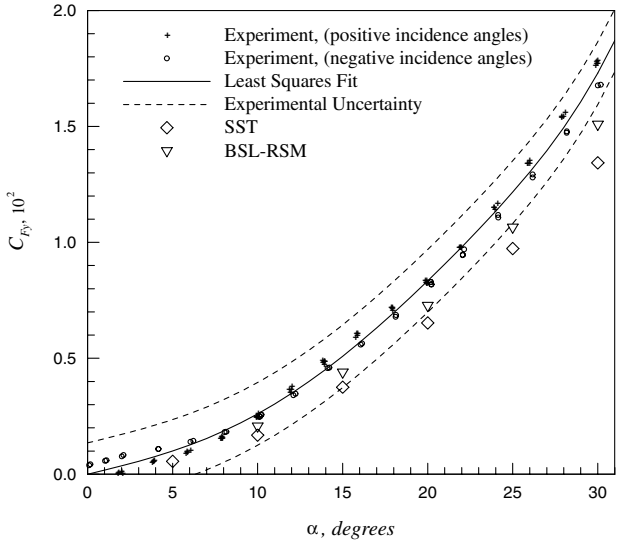

a) DRDC-STR hull, *Re* = 23 million

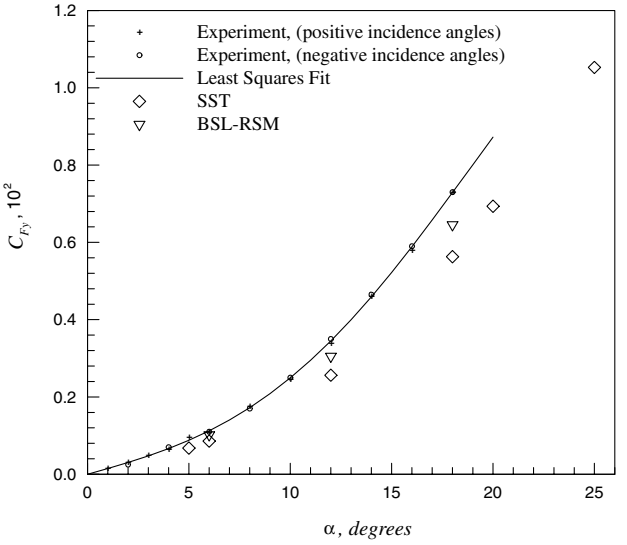

b) Series-58 model 4621 hull, *Re* = 11.7 million

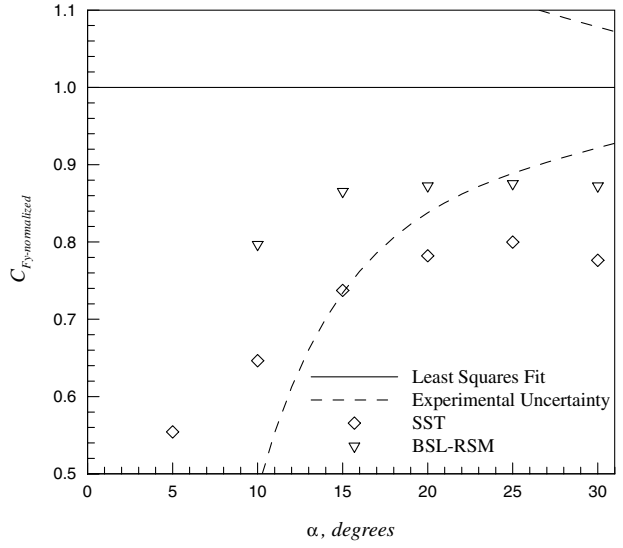

c) DRDC-STR normal force normalized by the least squares fit to the experimental data, *Re* = 23 million

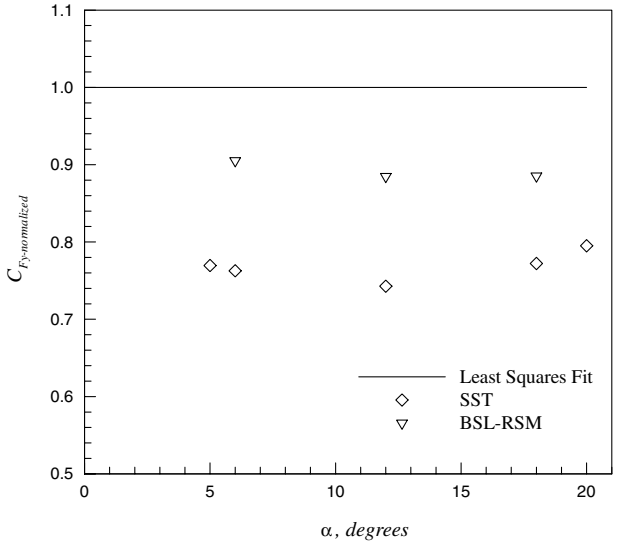

d) Series-58 model 4621 normal force normalized by the least squares fit to the experimental data, *Re* = 11.7 million

Fig. 7 Overall normal force coefficient for both experiment and RANS predictions as a function of incidence angle and turbulence model.

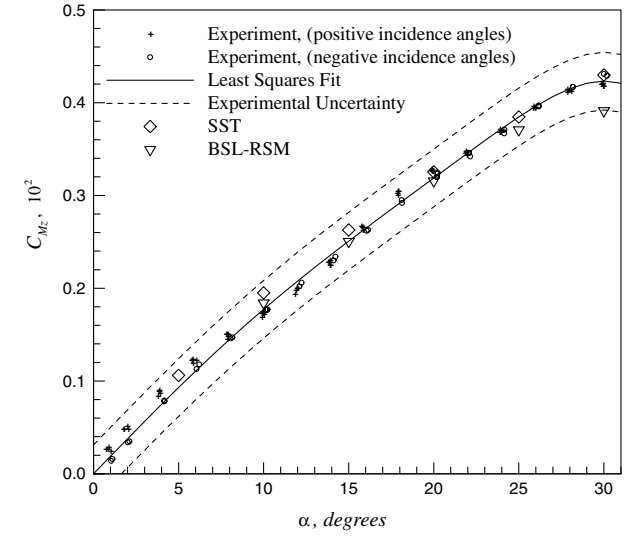

a) DRDC-STR hull at *Re* = 23 million

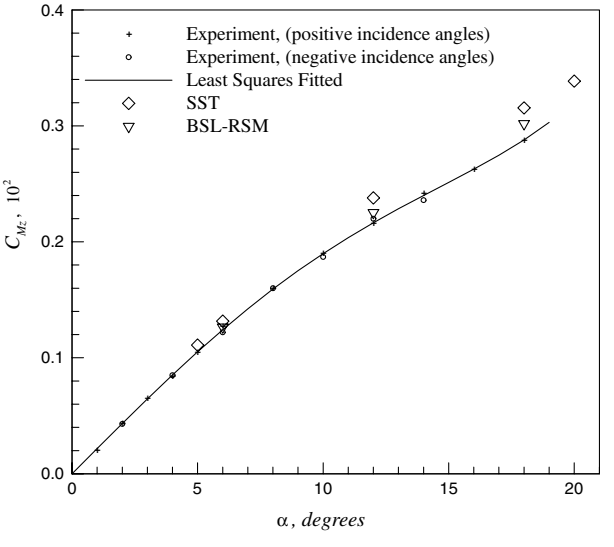

b) Series-58 model 4621 hull at *Re* = 11.7 million

Fig. 8 Overall pitching-moment coefficient for both experiment and RANS predictions as a function of incidence angle and turbulence model.

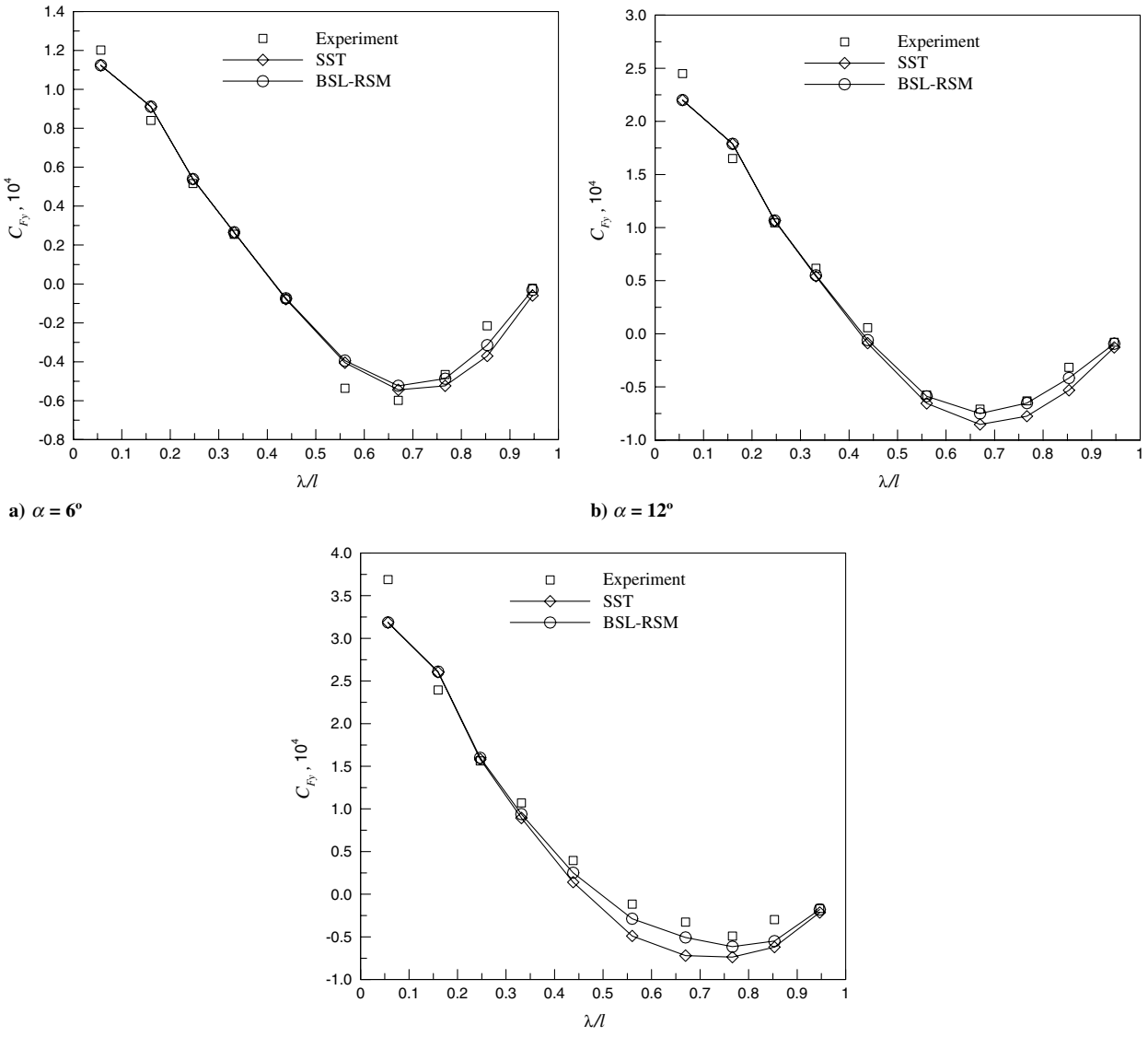

Fig. 9 Comparison of segmented normal force between experimental results and RANS predictions for the Series-58 model 4621 hull at $Re = 11.7 \times 10^6$.

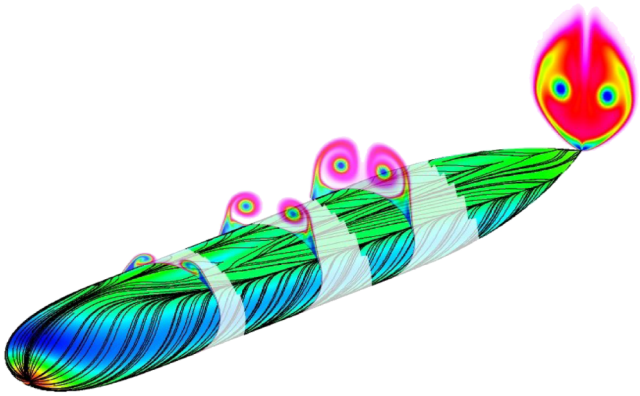

Fig. 10 A contour of surface-pressure and skin-friction lines for the DRDC-STR geometry at $Re = 23 \times 10^6$ and $\alpha = 30$ deg using the BSL-RSM turbulence model.

correspond to $\theta = 0$ and 180 deg, respectively. Pressure is plotted in terms of the crossflow pressure coefficient C_{pc}, which is normalized using the crossflow velocity $|U_\infty| \sin(\alpha)$. Using this definition, values greater than one are possible due to the axial component of the flow. The general shape of the RANS predictions are similar to measured distributions around a 6:1 spheroid [34].

Circumferential surface-pressure distributions over the nose region are shown in Fig. 11a. The pressure distributions are initially similar to a transient two-dimensional cylinder impulsively started from rest (if dimensionless time were substituted for λ/l) [35]. At $\lambda/l = 0.01$ and 0.02, the pressure distribution tends from a high pressure on the windward side to a strong suction on the leeward side. At $\lambda/l = 0.01$, $C_{pc} = 4$ on the windward side, which corresponds to a stagnation point based on the total flow. Further aft, at $\lambda/l = 0.10$, the high-pressure region on the windward side diminishes to the stagnation pressure based on the crossflow, and the suction on the leeward side migrates to $\theta = 90$ deg, where $C_{pc} \approx -3$, which is comparable with the result for plane potential flow over a cylinder. At $\lambda/l = 0.20$, the leeside pressure recovery is halted from $\theta \approx 135$–155 deg, indicating flow separation.

Circumferential surface-pressure distributions over the midbody and tail regions are shown in Figs. 11b and 11c, respectively. The maximum suction continually diminishes and moves windward due to boundary-layer growth. The primary pressure recovery on the leeside is reduced due to flow separation and the presence of the trailing vortices. A secondary leeside pressure recovery occurs because of a secondary reattachment of the flow due to the presence of the leeside vortices.

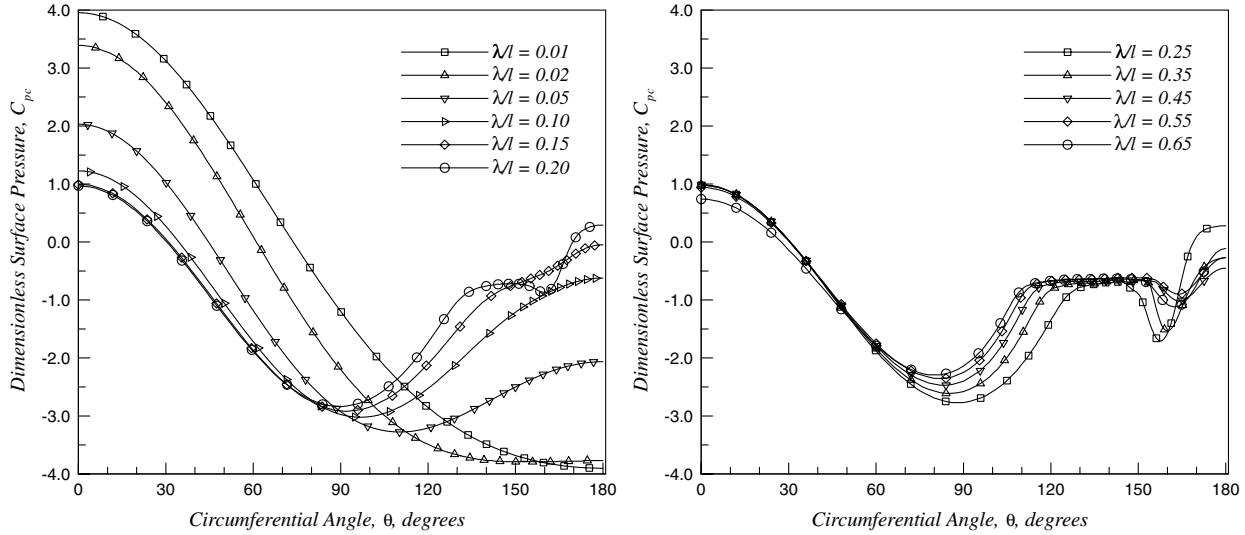

a) Nose region

b) Midbody region

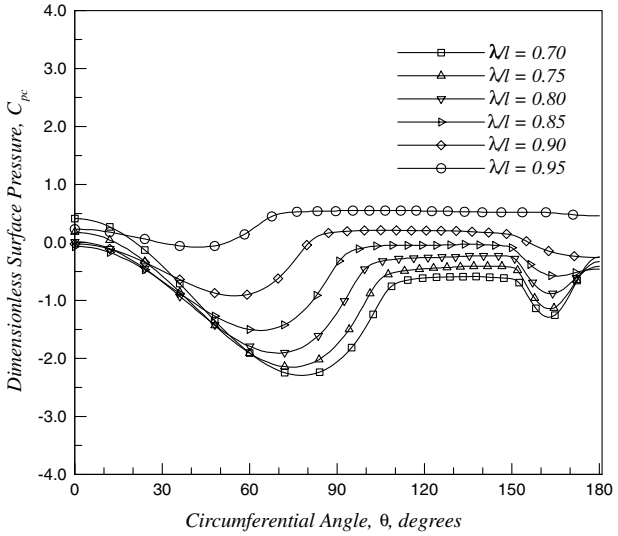

c) Tail region

Fig. 11 Circumferential variation of surface pressure at constant axial locations based on BSL-RSM RANS predictions for the DRDC hull at $Re = 23 \times 10^6$ and $\alpha = 30$ deg, (every sixth data point is shown).

The normal force was determined by integrating surface pressure and wall shear stress; however, it was found that the wall shear contribution is practically negligible and therefore virtually all of the normal force can be attributed the pressure distributions shown in Fig. 11.

Wall shear stress is an indicator of larger wall-normal velocities [33], the defining trait of separation for these types of flows [31]. However, for practical purposes, flow separation from axisymmetric bodies at moderate incidence is located near minimums in wall shear stress magnitude [33]. BSL-RSM RANS predictions of circumferential skin friction at constant axial locations are plotted in Fig. 12 for the DRDC hull at $Re = 23 \times 10^6$ and $\alpha = 30$ deg in normalized form, where $|C_f|$ is the magnitude of wall shear stress, normalized by the freestream dynamic pressure. The shape of these distributions compare well with those measured by Wetzel and Simpson [33] and Wetzel [36] for a 6:1 prolate spheroid. Local minimums in the circumferential skin-friction distributions indicate flow separation. From Fig. 12, at $\lambda/l = 0.01$, 0.02, 0.05, and 0.10, $|C_f|$ has no minimum and therefore the flow remains attached in this region. At $\lambda/l = 0.15$, a minimum is visible at $\theta \approx 150$ deg, indicating that the flow has separated. A primary minimum that continually migrates windward is evident in all the remaining $|C_f|$ distributions. For all the distributions in which $\lambda/l > 0.25$, a secondary minimum occurs between $\theta \approx 145$–150 deg, indicating a secondary separation.

Minimums in skin-friction magnitude of the RANS predictions were used to determine primary flow separation lines. Results based on the BSL-RSM RANS predictions are plotted in Fig. 13 for the DRDC-STR hull at $Re = 23 \times 10^6$ and $\alpha = 10$, 20, and 30 deg and for the Series-58 model 4621 hull at $Re = 11.7 \times 10^6$ and $\alpha = 6$, 12, and 18 deg. The initial separation point moves noseward as incidence is increased. Once the flow has separated, the separation line migrates continuously windward further aft. At a given axial position, separation occurs earlier as incidence is increased. Comparing Figs. 13a and 13b, it is clear that the primary separation is body-profile-dependent. These conclusions are in agreement with the conclusions of Ahn [34] and Wetzel [36] for a prolate spheroid.

VII. Normal Force Distributions and an Evaluation of Slender-Body Theory

The objective of this section is to evaluate slender-body theory as a tool for devising a hull force-estimation method. Both the normal force and pitching moment on our streamlined bodies can be determined by integration of the normal force distribution dF_y/dx,

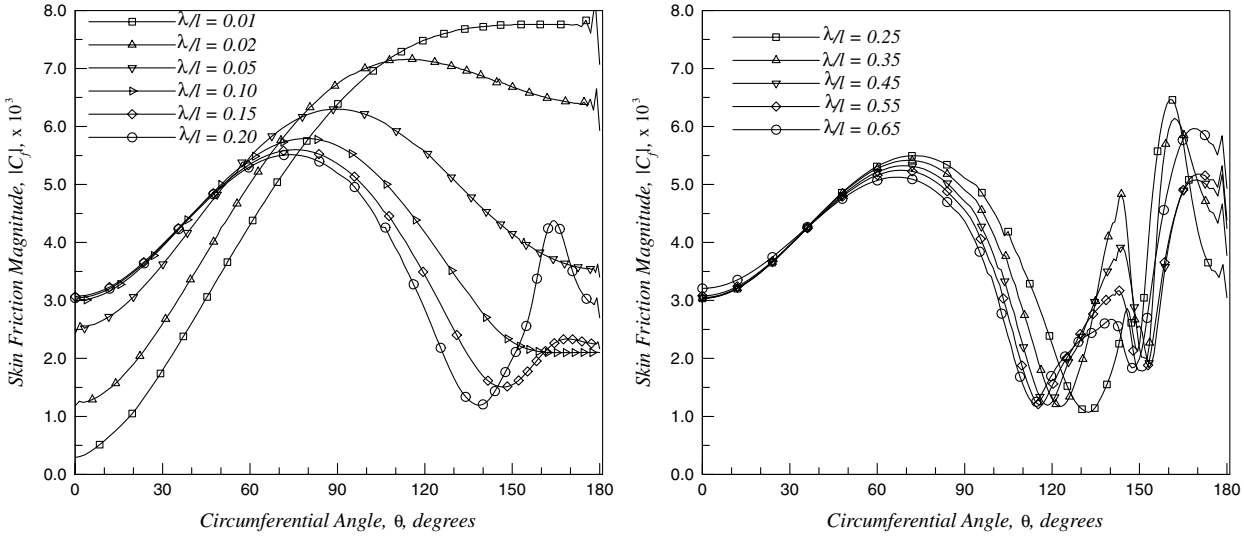

a) Nose region **b) Midbody region**

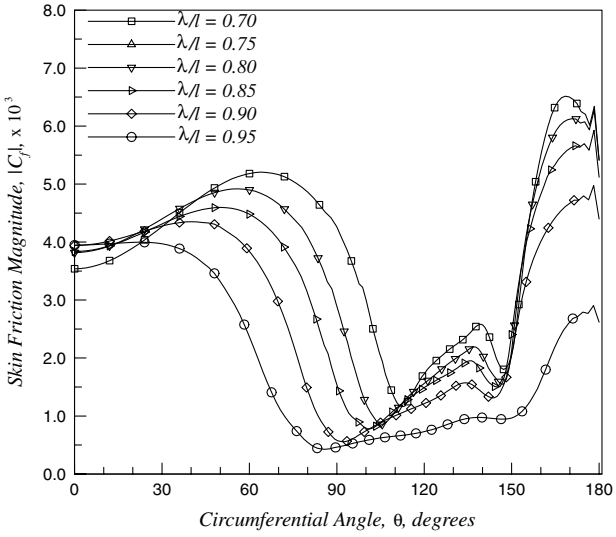

c) Tail region

Fig. 12 BSL-RSM RANS predictions of circumferential variation of skin-friction magnitude at constant axial locations for the DRDC hull at $Re = 23 \times 10^6$ and $\alpha = 30$ deg, (every sixth data point is shown).

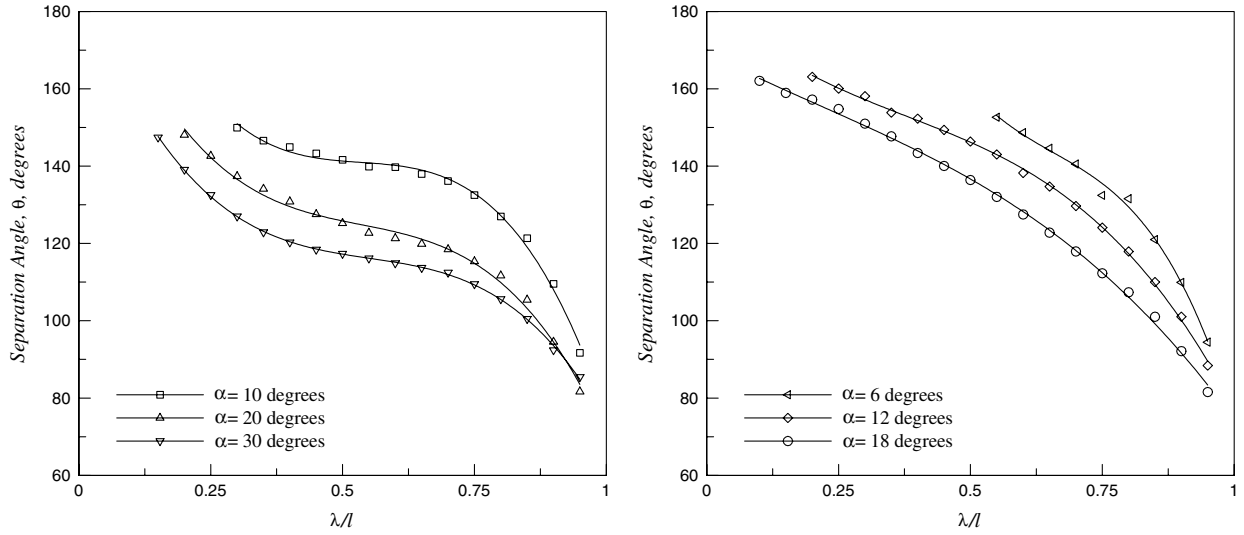

a) DRDC-STR, *Re* = 23 million **b) Series-58, *Re* = 11.7 million**

Fig. 13 BSL-RSM RANS predictions of primary separation lines for both the DRDC-STR and Series-58 hulls as a function of incidence.

which is the normal force per unit length along the longitudinal or x axis. At a given axial location, the normal force per unit length is determined by integrating the circumferential surface-pressure and skin-friction distributions predicted by RANS simulations. Dimensionless normal force distributions C_n are shown in Fig. 14, based on BSL-RSM RANS predictions for the DRDC-STR hull at $Re = 23 \times 10^6$ and $\alpha = 10$, 20, and 30 deg and for the Series-58 model 4621 hull at $Re = 11.7 \times 10^6$ and $\alpha = 6$, 12, and 18 deg.

All of the viscous normal force distributions exhibit the same shape: that is, a large upward force over the nose, an upward force over the midbody, and a downward force over the tail. In terms of the crossflow hydrodynamics, the upward force over the nose is due to the expanding body radius, which causes a source effect that increases the pressure on the windward side of the body. The upward force along the midbody is due to separation and the presence of leeside vortices, which redirects the flow and inhibits any pressure recovery on the leeside. The downward force along the tail region is due to the collapsing body radius, which causes a sink effect that decreases the pressure on the windward side and increases the pressure on the leeward side. However, this downward force is not as large as predicted by inviscid flow models, because the leeside vortices inhibit the flow contraction by reducing the pressure recovery on the leeside.

It is evident from Fig. 14 that the normal force distribution is dependent on both incidence and body shape. As suggested by Munk [1], the ordinate in Fig. 14 has been further scaled by $\sin(2\alpha)$, which is exact for potential flow over axisymmetric bodies. For a given body profile, this collapses the normal force distribution over the nose region at various angles of incidence, indicating that this scaling law is correct in this region. However, once the flow separates, the distributions deviate from one another, depending on incidence. As incidence increases, the upward normal force on the midbody increases, whereas the downward force on the tail decreases. The combined effect is a significant normal force and pitching moment that vary nonlinearly with incidence.

Slender-body theory provides a method of calculating the normal force distribution based on the hydrodynamic impulse. Jones [37] introduced the assumption that normal force in a cross-sectional plane through a slender body is generated only if the fluid particles are accelerated relative to an observer fixed in inertial space. Consider the flow in the fixed plane shown in Fig. 15. As the body passes through this plane, the flowfield and hence the impulse are functions of time. Jones related the time derivative of the hydrodynamic impulse in this plane to the spatial derivative of the body-fixed coordinate system as follows:

$$\frac{\mathrm{d}F_y(x)}{\mathrm{d}x} = \rho \frac{\mathrm{d}}{\mathrm{d}x}(i_Y(x))\frac{\mathrm{d}x}{\mathrm{d}t} \tag{4}$$

where $\mathrm{d}x/\mathrm{d}t = |U_\infty|\cos\alpha$ is the rate at which the body passes through the stationary plane, and $i_Y(x)$ is the longitudinal distribution of hydrodynamic impulse per unit length parallel to the y axis, defined as

$$i_Y(x) = \frac{\mathrm{d}I_Y}{\mathrm{d}X} = \int_{-\infty}^{\infty}\int_{-\infty}^{\infty} v_i(x)\rho \mathrm{d}y\mathrm{d}z \tag{5}$$

Thus, the normal force distribution along the body is proportional to the axial rate of change of this hydrodynamic impulse distribution.

The total normal force F_y on the body is derived from Eq. (4) by integration over the body length l to give

$$F_y = \rho|U_\infty|\cos\alpha i_Y(l) \tag{6}$$

because i_Y is zero at the nose. That is, the total normal force is just proportional to the hydrodynamic impulse in the tail plane located at $\lambda = l$. The pitching moment about the tail, $M_{z\,\mathrm{tail}}$, is derived from integration of the moment of Eq. (4) over the body length as follows:

$$M_{z\,\mathrm{tail}} = \rho|U_\infty|\cos\alpha\int_0^l i_Y(x)\mathrm{d}x \tag{7}$$

Thus, $M_{z\,\mathrm{tail}}$ is proportional to the area under the normal impulse axial distribution.

Jones [37] considered unseparated flows around slender wings and was able to calculate the impulse from potential-flow theory. In the present case, the flow is viscous and separated from the body, and so the impulse of Eq. (5) can be calculated from the velocity field of the CFD solution. However, an alternative approach suggested by Howe [38] and Lamb [39] is also considered. It states that the hydrodynamic impulse for the moving body in Fig. 15, as defined in Eq. (5), can be expressed in terms of the vorticity field as follows:

$$i_Y(x) = \int_{-\infty}^{\infty}\int_{-\infty}^{\infty}(\omega_x z)\mathrm{d}y\mathrm{d}z - \pi a^2|U_\infty|\sin\alpha \tag{8}$$

When primary flow separation occurs, vorticity developed in the boundary layer flows into the outer flowfield, forming two concentrated vortices. Therefore, viscous effects can be interpreted and possibly modeled by the presence of vorticity in the wake using Eq. (8). Rendered contours of ω_x predicted by BSL-RSM RANS simulations are shown in Fig. 16a for the DRDC-STR hull at $Re =$

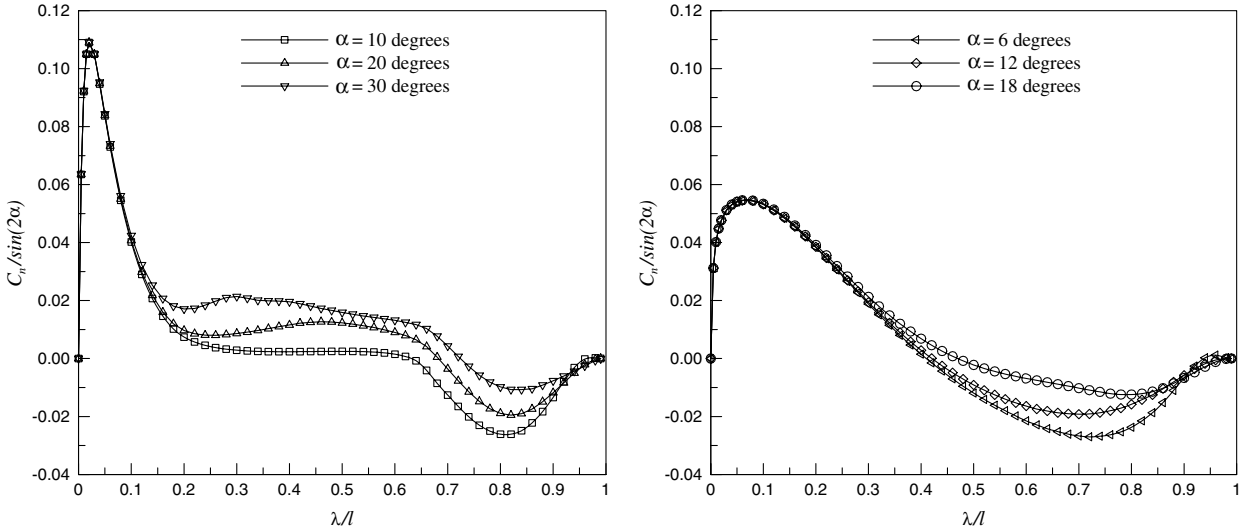

a) DRDC-STR hull, *Re* = 23 million **b) Series-58 hull, *Re* = 11.7 million**

Fig. 14 Distributions of normal force per unit length based on BSL-RSM RANS predictions.

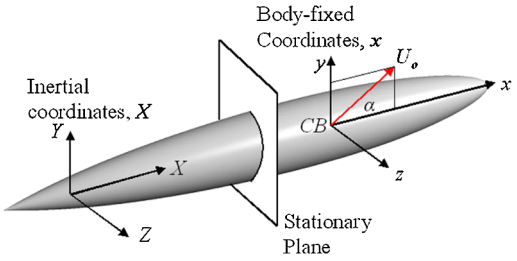

Fig. 15 Body with inertial and body-fixed coordinates.

23×10^6 and $\alpha = 30$ deg. The distributions are plotted in the y–z plane at successive axial locations. Initially, in the nose region, all the vorticity is located in a thin sheet around the body circumference. As the flow progresses over the nose, this sheet thickens on the leeside due to diffusion. Once the flow separates, vorticity is shed from the boundary layer in two shear layers located on the sides of the body and convected into the outer flowfield. This vorticity rolls up into two concentrated vortices on the leeside. Along the midbody and tail regions the shear layers continually feed these two vortices, causing them to grow in size and strength. In addition, a secondary separation occurs and secondary vortices of opposite sign develop between the body and the primary vortices. The primary vortices remain attached until $\lambda/l = 1.0$, at which point they are freed and swept away with the freestream. As shown in Fig. 16, the primary difference between the SST and the BSL-RSM simulations is that the SST simulation is more dissipative along the tail region.

Circulation describes the flow of vorticity and is often used to measure the strength of a vortex. The circulation of the vorticity field in the half-plane is determined from the area integration:

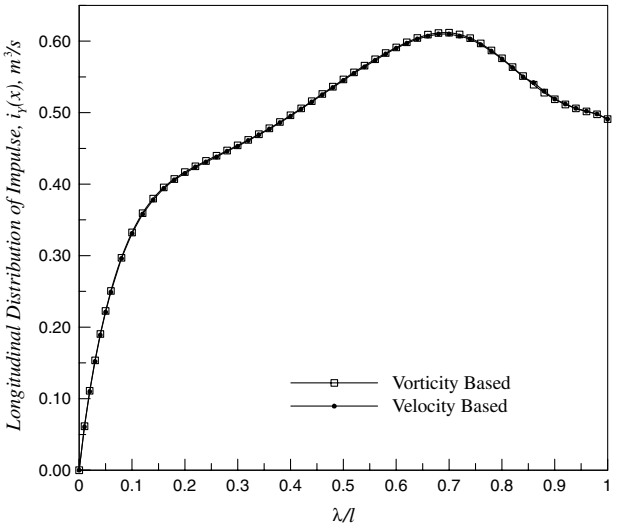

Fig. 17 Longitudinal distributions of hydrodynamic impulse per unit length parallel to the y axis determined using both the velocity and vorticity field of the BSL-RSM RANS predictions for the DRDC-STR hull at $\alpha = 20$ deg, and $Re = 23 \times 10^6$.

$$\Gamma(x) = \int_o^\infty \int_{-\infty}^\infty \omega_x(x)\mathrm{d}y\mathrm{d}z \tag{9}$$

The circulation over the full plane is zero by symmetry.

Using these RANS predictions, longitudinal distributions of impulse per unit length parallel to the y axis were determined based

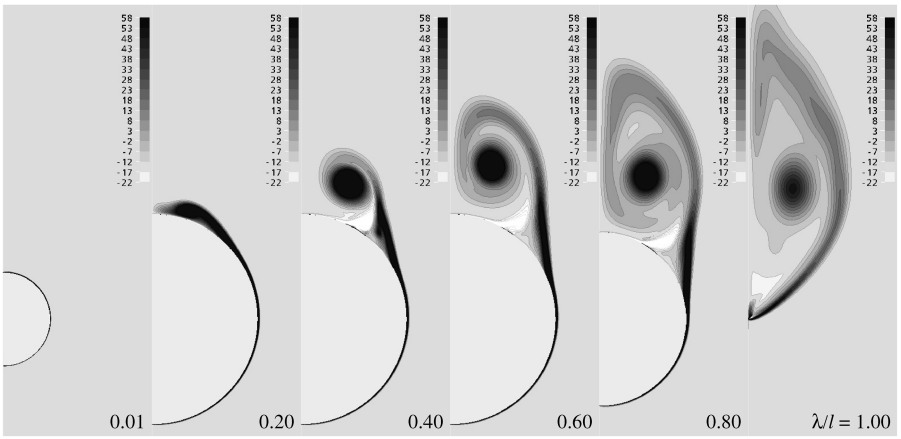

a) BSL-RSM turbulence model

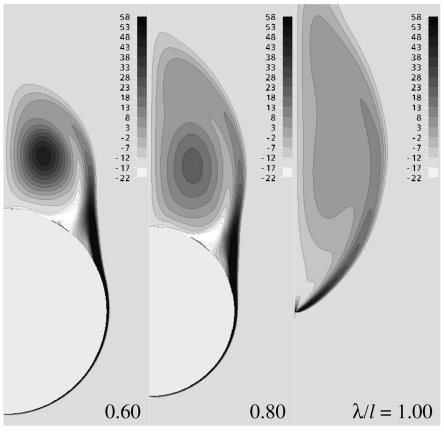

b) SST turbulence model

Fig. 16 RANS predictions of ω_x distributions at various axial locations for the DRDC-STR hull at $Re = 23 \times 10^6$ and $\alpha = 30$ deg.

on the velocity field using Eq. (5) and the vorticity field using Eq. (8). Plotted in Fig. 17 are predictions based on the BSL-RSM RANS results for the DRDC-STR hull at $\alpha = 20$ deg and $Re = 23 \times 10^6$. It is evident that both methods result in nearly identical distributions of hydrodynamic impulse $i_Y(x)$.

Additional axial distributions of hydrodynamic impulse determined from the x component of vorticity are shown in Fig. 18 based on BSL-RSM RANS predictions for both the DRDC-STR and Series-58 model 4621 hull. The impulse is normalized by crossflow velocity and body length squared. The general shape of all the impulse distributions in Fig. 18 is similar. The hydrodynamic impulse increases rapidly over the forebody, and before separation the curves for a given body shape are identical. However, after separation the hydrodynamic impulse at a given axial location is consistently greater as incidence is increased. The hydrodynamic impulse then reaches a maximum and declines over the afterbody, leaving a residual impulse at the tail. In a potential-flow solution the impulse returns to zero at the end of the body, leaving behind no residual impulse. As incidence is increased so too does the impulse left in the wake. It is also interesting to note that over the midbody region of the DRDC-STR hull, which has a constant body diameter, the hydrodynamic impulse increased approximately linearly.

Normal force and pitching moment were predicted based on the hydrodynamic impulse distributions in Fig. 18 using Eqs. (6) and (7), respectively. Shown in Fig. 19 is a comparison of these predictions to the exact-numerical predictions derived from the integration of surface pressure and skin friction and using no slender-body assumptions. These results are based on the BSL-RSM RANS predictions for the DRDC-STR hull at $Re = 23 \times 10^6$. To give an estimate of the relative error between these two methods, experimental data are also shown. It is evident that force and moment predictions using both methods are nearly identical at all incidences, with the possible exception of $\alpha = 30$ deg, and the relative error between the two is small compared with error in the experimental data. Thus, Eqs. (6) and (7) are validated and the slender-body assumption is justified for these body shapes in the range of incidence considered.

Normal force distributions were also predicted based on the hydrodynamic impulse distributions in Fig. 18 using Eq. (4). Shown in Fig. 20 is a comparison of these predictions with those determined

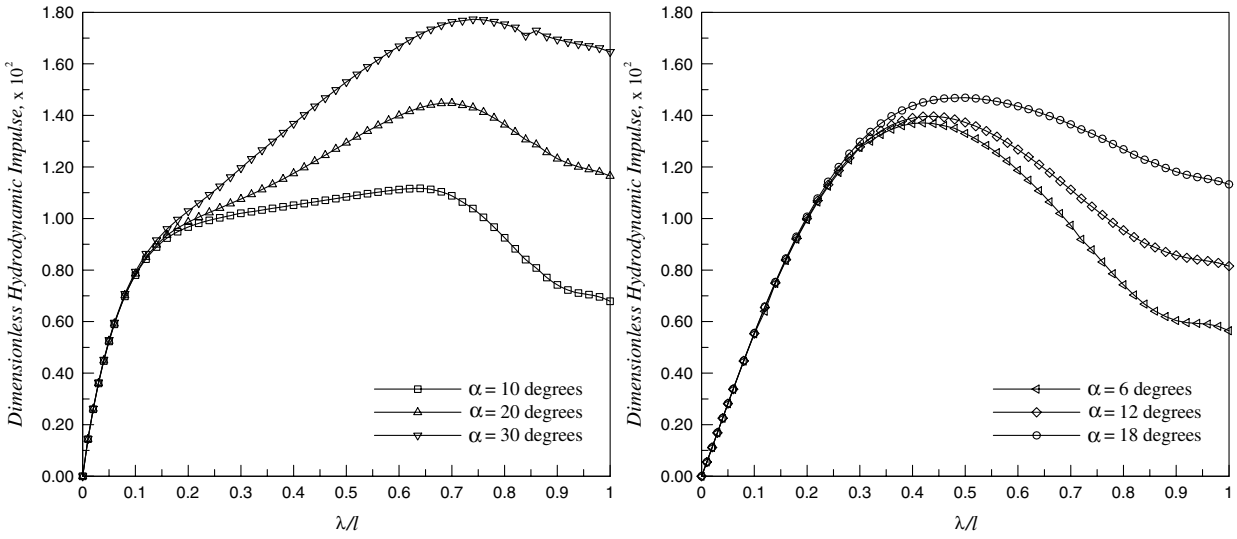

a) DRDC-STR hull, *Re* = 23 million **b) Series-58 model 4621 hull, *Re* = 11.7 million**

Fig. 18 Longitudinal distributions of hydrodynamic impulse parallel to the *y* axis based on the vorticity field of RANS predictions using the BSL-RSM turbulence model.

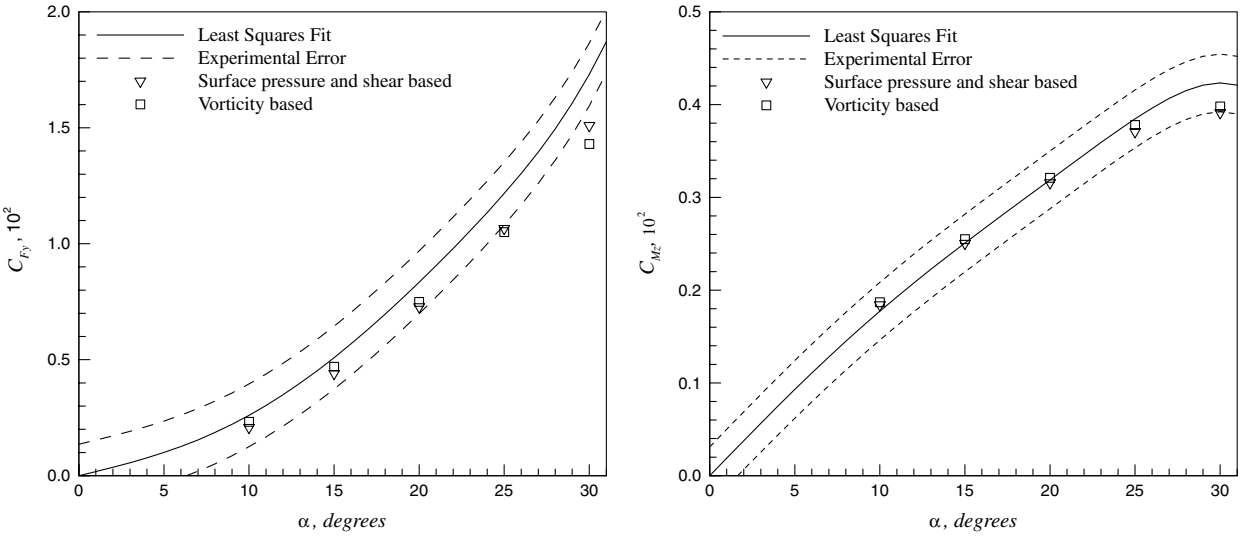

a) Normal force **b) Pitching moment about center of buoyancy**

Fig. 19 A comparison of normal force and pitching-moment predictions determined by integrating surface pressure and shear to those determined using the *x* component of vorticity. Based on BSL-RSM RANS predictions for the DRDC-STR hull at $Re = 23 \times 10^6$.

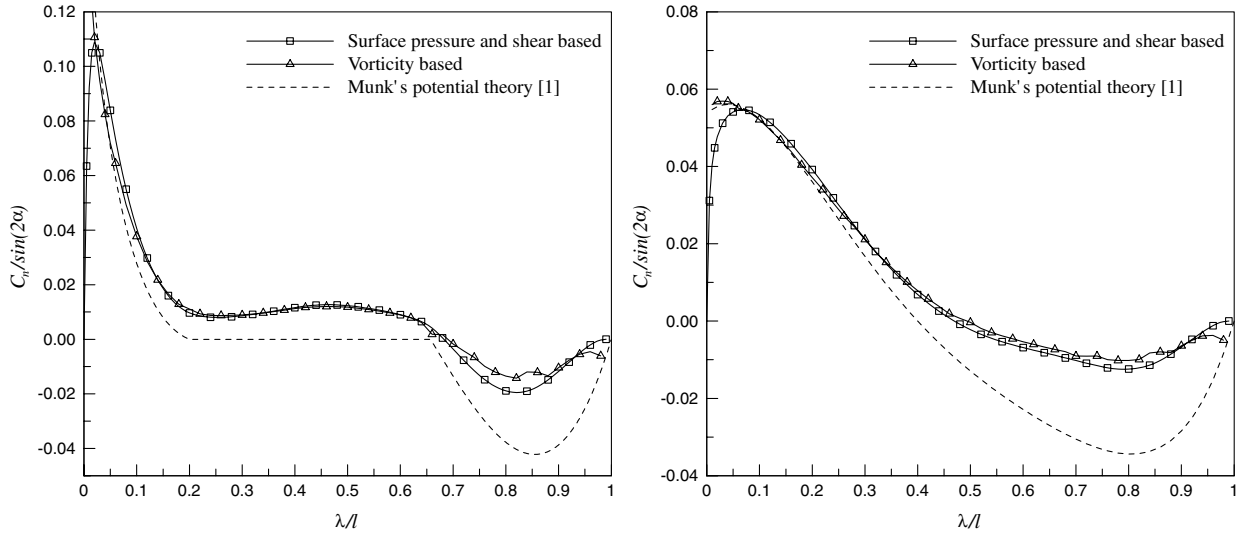

a) DRDC-STR, *Re* = 23 million and α = 20º **b) Series-58 model 4621, *Re* = 11.7 million and α = 18º**

Fig. 20 A comparison of normal force distributions determined by integrating surface pressure and shear to those determined using the *x* component of vorticity. Based on BSL-RSM RANS predictions (every second data point is shown).

by integrating surface pressure and skin friction (no slender-body assumptions used). Results are based on the BSL-RSM RANS predictions for DRDC-STR hull at $Re = 23 \times 10^6$ and $\alpha = 20$ deg and for Series-58 model 4621 hull at $Re = 11.7 \times 10^6$ $\alpha = 18$ deg. To help assess the relative error between these two methods, normal force distributions based on Munk's [1] potential-flow theory are also shown. It is evident that both viscous normal force distributions compared very favorably and the error between them is small compared with Munk's potential-flow predictions. Slight differences do occur, especially near the nose and tail, and this is likely due to the inadequacy of the slender-body approximation made in Eq. (4).

The preceding results clearly show that the hydrodynamic impulse distributions of Fig. 18 have three physical interpretations that lend themselves well to hydrodynamic force modeling. The first is that the normal force is directly proportional to the normal component of hydrodynamic impulse per unit length in the tail plane (i.e., at $\lambda/l = 1.0$). The second is that the pitching moment about the tail is directly proportional to the area under the distribution of hydrodynamic impulse per unit length. The third is that the normal force distribution is directly proportional to the axial rate of change of the hydrodynamic impulse distribution.

VIII. Conclusions

A comprehensive computational study was performed on two slender axisymmetric bodies at moderate-to-large incidence using a RANS solver. Hybrid meshes were generated using a scripted algorithm that provided good discretization of the leeside vortex and near-wall shear layers. Overall force and moment predictions are within experimental uncertainty up to 25 deg incidence. Normal force distributions show close agreement with experimental data.

Both SST and BSL-RSM turbulence models were evaluated. The BSL-RSM turbulence model was superior to the SST model at predicting the normal force and moment, reducing modeling error by approximately 50%. The BSL-RSM model consistently predicted earlier separation and increased energy loss in the leeside vortex, resulting in increased normal force predictions at a given incidence without significantly altering moment predictions. Although the total circulation of the leeside vortex is nearly identical for both models, the BSL-RSM model predicts less diffusion, resulting in a more concentrated vortex.

Using the slender-body assumption, normal force distributions were estimated from the axial distribution of hydrodynamic impulse using only the longitudinal component of the RANS vorticity field. These distributions compared favorably with those determined by direct integration of surface pressure and shear stress and provided reliable predictions of normal force and pitching moment in these viscous separated flows.

These results are being used to develop improved force-estimation methods for streamlined axisymmetric bodies.

Acknowledgments

This work has been funded through a contract with Defence Research and Development Canada and through the Natural Sciences and Engineering Research Council Discovery Grants of authors Gerber and Holloway. The authors would also like to acknowledge QinetiQ and the United Kingdom Ministry of Defence for their contribution to the baseline Reynolds stress model Reynolds-averaged Navier–Stokes simulations on the Series-58 model 4621 hull, the Institute for Aerospace Research, National Research Council Canada, for their contributions to Defence Research and Development Canada static-test-rig experiments, and the U.S. Naval Surface Warfare Center Carderock Division for sharing the Series-58 model 4621 data.

References

[1] Munk, M. M., "The Aerodynamic Forces on Airship Hulls," NACA Rept. 184, 1924.

[2] Watt, G. D., Tanguay, B., and Cooper, K. R., "Submarine Hydrodynamics in the Wind Tunnel: The DREA Static Test Rig," *Warship '91: Royal Institution of Naval Architects International Symposium on Naval Submarines 3*, Royal Inst. of Naval Architects, London, May 1991.

[3] Watt, G. D., Nguyen, V. D., Cooper, K. R., and Tanguay, B., "Wind Tunnel Investigations of Submarine Hydrodynamics: The Development of the DREA Static Test Rig and Some Results," *Canadian Aeronautics and Space Journal*, Vol. 39, No. 3, 1993, pp. 119–126.

[4] Nguyen, V. D., Drolet, Y., and Watt, G. D., "Interference of Various Support Strut Configurations in Wind Tunnel Tests on a Submarine Model," 33rd Aerospace Sciences Meeting and Exhibit, AIAA Paper 95-0443, Jan. 1995.

[5] Van Randwijck, E. F., and Feldman, J. P., "Results of Experiments with a Segmented Model to Investigate the Distribution of the Hydrodynamic Forces and Moments on a Streamlined Body of Revolution at an Angle of Attack or with a Pitching Angular Velocity," Naval Surface Warfare Center Carderock Division, NSWCCD-50-TR-2000/008, Bethesda, MD, Feb. 2000.

[6] Pankajakshan, R., Remotigue, M. G., Taylor, L. K., Jiang, M., Briley, W. R., and Whitfield, D. L., "Validation of Control-Surface Induced Submarine Manoeuvring Simulations Using UNCLE," *24th Symposium on Naval Hydrodynamics*, Naval Studies Board, Office of Naval Research, Washington, D.C., July 2002, pp. 624–639.

[7] Sung, C. H., Rhee, B., and Koh, I. Y., "Validation of Forces, Moments and Stability Derivatives of a Maneuvering Series-58 Bare Hull,"

25th Symposium on Naval Hydrodynamics, Vol. 5, Naval Studies Board, Office of Naval Research, Washington, D.C., Aug. 2004, pp. 19–30.

[8] Baker, C. R., Jeans, T. L., Gerber, A. G., Holloway, A. G. L., and Watt, G. D., "Examination of the Flow Separation Characteristics Around a Streamlined Axisymmetric Shape," 2005 ASME Fluids Engineering Division Summer Meeting and Exhibition, Houston, TX, American Society of Mechanical Engineers Paper FEDSM 2005-77149, June 2005.

[9] Forsythe, J. R., Squires, K. D., Wurtzler, K. E., and Spalart, P. R., "Detached Eddy Simulation of Fighter Aircraft at High Alpha," 40th AIAA Aerospace Sciences Meeting and Exhibit, AIAA Paper 2002-0591, Jan. 2002.

[10] Morton, S. A., Steenman, M. B., Cummings, R. M., and Forsythe, J. R., "DES Grid Resolution Issues for Vortical Flows on a Delta Wing and an F18C," 41st AIAA Aerospace Sciences Meeting and Exhibit, AIAA Paper 2003-1103, Jan. 2003.

[11] Mitchell, A. M., Morton, S. A., Forsythe, J. R., and Cummings, R. M., "Analysis of Delta-Wing Vortical Substructures Using Detached-Eddy Simulation," *AIAA Journal*, Vol. 44, No. 5, May 2006, pp. 964–972.

[12] Nichols, R. H., "Algorithm and Turbulence Model Requirements for Simulating Vortical Flows," 46th AIAA Aerospace Sciences Meeting and Exhibit, AIAA Paper 2008-337, Jan. 2008.

[13] Menter, F. R., and Kuntz, M., "Adaptation of Eddy-Viscosity Turbulence Models to Unsteady Separated Flow Behind Vehicles," *Aerodynamics of Heavy Vehicles: Trucks, Busses and Trains*, edited by R. McCallen, F. Browand, J. Ross, Springer, New York, 2004.

[14] Degani, D., "Effect of Geometrical Disturbance on Vortex Asymmetry," *AIAA Journal*, Vol. 29, No. 4, 1991, pp. 560–566. doi:10.2514/3.59929

[15] Schiff, L. B., Degani, D., and Cummings, R. M., "Computation of Three-Dimensional Turbulent Vortical Flows on Bodies at high Incidence," *Journal of Aircraft*, Vol. 28, No. 11, 1991, pp. 689–699. doi:10.2514/3.46084

[16] Degani, D., and Levy, Y., "Asymmetric Turbulent Vortical Flows over Slender Bodies," *AIAA Journal*, Vol. 30, No. 9, 1992, pp. 2267–2273. doi:10.2514/3.11214

[17] Allen, H. J., and Perkins, E. W., "Characteristics of Flow over Inclined Bodies of Revolution," NACA RM A50L07, 1951.

[18] Lamont, P. J., "Pressures Around an Inclined Ogive Cylinder with Laminar, Transitional, or Turbulent Separation," *AIAA Journal*, Vol. 20, No. 11, 1982, pp. 1492–1499. doi:10.2514/3.51212

[19] Ericsson, L. E., and Reding, J. P., "Vortex-Induced Asymmetric Loads in 2D and 3D Flows," 18th AIAA Aerospace Sciences Meeting, Pasadena, CA, AIAA Paper 1980–181Jan. 1980.

[20] Ferziger, J. H., and Peric, M., *Computational Methods for Fluid Dynamics*, 2nd ed., Springer, Berlin, 1999.

[21] Menter, F. R., "Two-equation Eddy Viscosity Turbulence Models For Engineering Application," *AIAA Journal*, Vol. 32, No. 8, 1994, pp. 1598–1605. doi:10.2514/3.12149

[22] Launder, B. E., Reece, G. J., and Rodi, W., "Progress in the Development of a Reynolds-Stress Turbulence Closure," *Journal of Fluid Mechanics*, Vol. 68, No. 3, Apr. 1975, pp. 537–566.

[23] Schneider, G. E., and Raw, M. J., "Control-Volume Finite Element Method for Heat Transfer and Fluid Flow Using Co-Located Variables, Part 1: Computational Procedure," *Numerical Heat Transfer*, Vol. 11, No. 4, 1987, pp. 363–390. doi:10.1080/10407788708913560

[24] Hutchinson, B. R., Galpin, P. F., and Raithby, G. D., "Application of Additive Correction Multi-Grid to the Coupled Fluid Flow Equations," *Numerical Heat Transfer*, Vol. 13, No. 2, 1988, pp. 133–147. doi:10.1080/10407788808913608

[25] Raw, M. J., "A Coupled Algebraic Multi-Grid method for the 3D Navier-Stokes Equations," *Notes on Numerical Fluid Mechanics*, Vol. 49, Vieweg-Verlag, Braunschweig, Germany, 1995.

[26] Hutchinson, B. R., and Raithby, G. D., "A Multi-Grid Method Based on the Additive Correction Strategy," *Numerical Heat Transfer*, Vol. 9, 1986, pp. 511–537. doi:10.1080/10407788608913491

[27] Raw, M. J., "Robustness of Coupled Algebraic Multi-Grid for the Navier-Stokes Equation," 34th Aerospace and Sciences Meeting and Exhibit, Reno, NV,AIAA Paper 96-0297, Jan. 1996.

[28] Baker, C. R., "A Strategic Meshing Approach to Modeling Hydrodynamic Flow Around Streamlined Axisymmetric Shapes," Masters Thesis, Dept. of Mechanical Engineering, Univ. of New Brunswick, New Brunswick, Canada, Mar. 2006.

[29] Watt, G. D., Baker, C. R., Gerber, A. G., and Fouts, C., "Scripted Hybrid Mesh Adaptation for High Incidence RANS Flows About Axisymmetric Shapes," 44th AIAA Aerospace Sciences Meeting and Exhibit, Reno, NV, AIAA Paper 2006-886, Jan. 2006.

[30] Watt, G. D., Baker, C. R., and Gerber, A. G., "ANSYS CFX-10.0 RANS Normal Force Predictions for the Series-58 model 4621 Unappended Axisymmetric Submarine Hull in Translation," Defence Research and Development Canada—Atlantic, TM 2006-037, Dartmouth, NS, Canada, Sept. 2006.

[31] Simpson, R. L., "Aspects of Turbulent Boundary Layer Separation," *Progress in Aerospace Sciences*, Vol. 32, Nov. 1996, pp. 457–521. doi:10.1016/0376-0421(95)00012-7.

[32] Yates, L. A., and Chapman, G. T., "Streamlines, Vorticity Lines, and Vortices Around Three-Dimensional Bodies," *AIAA Journal*, Vol. 30, No. 7, 1992, pp. 1819–1826. doi:10.2514/3.11142

[33] Wetzel, T. G., and Simpson, R. L., "Measurement of Three-Dimensional Crossflow Separation," *AIAA Journal*, Vol. 36, No. 4, 1998, pp. 557–564. doi:10.2514/2.429

[34] Ahn, S., "An Experimental Study of Flow over a 6 to 1 Prolate Spheroid at Incidence," Ph.D. Dissertation, Aerospace Engineering Dept., Virginia Polytechnic Inst. and State Univ., Blacksburg, VA, 1992.

[35] Sarpkaya, T., "Separated Flow About Lifting Bodies and Impulsive Flow About Cylinders," *AIAA Journal*, Vol. 4, No. 3, 1966, pp. 414–420. doi:10.2514/3.3453

[36] Wetzel, T. G., "Unsteady Flow Over a 6 to 1 Prolate Spheroid," Ph.D. Dissertation, Aerospace Engineering Dept., Virginia Polytechnic Inst. and State Univ., Blacksburg, VA, 1996.

[37] Jones, R. T., "Properties of Low-Aspect-Ratio Pointed Wings at Speeds Below and Above the Speed of Sound," NACA Report No. 835, 1946.

[38] Howe, M. S., *Theory of Vortex Sound*, Cambridge Univ. Press, New York, 2002.

[39] Lamb, H., *Hydrodynamics*, 6th ed., Dover, New York, 1932.

J. Sahu
Associate Editor